Over-activation of BMP signaling in neural crest cells precipitates heart outflow tract septation

Jean-François Darrigrand[1], Mariana Valente[2], Pauline Martinez[1], Glenda Comai[3], Maxime Petit[4], Ryuichi Nishinakamura[5], Daniel S. Osorio[6], Vanessa Ribes[7], Bruno Cadot[1#].

1. INSERM - Sorbonne Université UMR974 - Center for Research in Myology, 105 boulevard de l'Hôpital, 75634 Paris Cedex 13, France.
2. Cellular, Molecular, and Physiological Mechanisms of Heart Failure team, Paris-Cardiovascular Research Center (PARCC), European Georges Pompidou Hospital (HEGP), INSERM U970, F-75737 Paris Cedex 15, France.
3. Stem Cells and Development, Department of Developmental & Stem Cell Biology, CNRS UMR 3738, Institut Pasteur, 25 rue du Dr. Roux, 75015 Paris, France.
4. Unité Lymphopoïèse – INSERM U1223, Institut Pasteur, 25 rue du Dr. Roux, 75015 Paris, France.
5. Institute of Molecular Embryology and Genetics, Kumamoto University, Japan.
6. Instituto de Investigação e Inovação em Saúde – i3S, Universidade do Porto, and Instituto de Biologia Molecular e Celular – IBMC, Porto, Portugal.
7. Institut Jacques Monod, CNRS UMR7592, Université Paris Diderot, Sorbonne Paris Cité, 75205 Paris Cedex, France.

corresponding author and lead contact: bruno.cadot@inserm.fr

Short title: BMPs and heart outflow tract

Summary

Establishment of separated pulmonary and systemic circulations in vertebrates relies on the key role of neural crest cells (NCC) for the septation of the embryonic cardiac outflow tract (OFT). Absence of NCCs induces OFT septation defects, analogous to a loss of Bone Morphogenetic Proteins (BMPs) activity, though it remains unclear how BMPs control cardiac NCC differentiation and behaviour. To address this question, we monitored cardiac NCC state upon gain in BMP signaling, caused by the deletion of *Dullard*, using 3D-imaging and single cell transcriptomics. Specific loss of *Dullard* in the NCC results in premature OFT septation, pulmonary artery obstruction and embryonic death. This is caused by uncontrolled NCC convergence towards the endocardium and asymmetrical myocardial differentiation, promoted by elevated levels of the guiding cue *Sema3c* and decreased levels in mesenchymal trait markers. Furthermore, we unraveled the molecular basis of the zipper-like OFT septation where graded Sema3c expression follow a gradient of BMP activation in NCC along the OFT length.

Keywords

Neural crest cells, Outflow tract, BMP signaling, Sema3c, Dullard

46 # Introduction

47

48 The embryonic OFT is a solitary tube called truncus arteriosus, which is remodelled into the aortic
49 (Ao) and pulmonary (Pa) arteries (1) (Fig. 1A). This morphogenesis is orchestrated in time and
50 space by several cross-interacting cell-types including the myocardial progenitors of the second
51 heart field (SHF), the endocardial cells (EC) delineating the OFT lumen, and the cardiac neural
52 crest cells (cNCC) (2,3) (Fig. 1A). Various genetic manipulations or ablations have highlighted the
53 predominant role of cNCC in initiating and controlling OFT septation (4,5). Originally, cNCC
54 delaminate from the dorsal neural tube and migrate through the pharyngeal mesoderm to reach
55 the developing OFT (Fig. 1A). They invade the two cardiac cushions, condense towards the
56 endocardium and trigger its rupture, thereby creating the two great arteries (6,7). The rupture of
57 the endocardium is first detected at the distal levels of the OFT, at E11.5 in mouse, and gets
58 progressively established at more proximal levels.

59

60 The intense investigations to identify the molecular cues controlling cNCC stereotyped behaviour
61 and differentiation in the OFT mesenchyme have established the importance of the Bone
62 Morphogenic Proteins (BMP), secreted by the outlying myocardium cells (8–10). Indeed, BMP
63 signaling loss-of-function within the NCC lineage leads to the formation of hypoplastic cushions,
64 a shorter and non-septated OFT, phenocopying the absence of cNCC (11–13). However, little is
65 known on the molecular cascades triggered by BMP signalling responsible for the cNCC mediated
66 OFT septation.

67

68 To get insights into these molecular cascades, we decided to dissect the role of Dullard (Ctdnep1)
69 during OFT morphogenesis, a perinuclear phosphatase uncovered as a BMP intracellular signaling
70 inhibitor (14–16). Dullard protein is evolutionary conserved from yeast to mammals. In xenopus,
71 drosophila and mouse embryos, it decreases the levels of phosphorylation of Smad1/5/8, the
72 downstream transcriptional effectors of BMP signalling (15–17).
73 We showed here that deletion of *Dullard* in the cNCC increases Smad1/5/8 activity, leading to
74 premature and asymmetric septation of the OFT, pulmonary artery closure and embryonic death.
75 This BMP overactivation in the cNCC triggers the downregulation of mesenchymal markers
76 (*Snai2*, *Twist1, Rac1, Mmp14* and *Cdh2*) and the upregulation of *Sema3c*, which in turn results in
77 premature cNCC compaction at the endocardium. In addition, asymmetric differentiation of the
78 distal subpulmonary myocardium contributes to OFT anisotropic rupture. Finally, our data
79 converge to a model whereby graded BMP activity and *Sema3c* expression in the cNCC along the
80 OFT axis set the tempo of OFT septation from its distal to its proximal regions. Hence, our findings
81 reveal that fine tuning of BMP signaling levels in cNCC orchestrate OFT septation in time and
82 space.
83

84 # Results

85

86 ### *Dullard* deletion triggers hyper-activation of BMP intracellular signalling in cNCC

87

88 In order to dig into BMP signalling functions during OFT septation, we decided to delete the
89 *Dullard* phosphatase in cNCC. Its role in inhibiting the BMP pathway was first confirmed in vitro
90 using the myogenic cell line C2C12, transfected with *Dullard* WT or *Dullard* with the phosphatase-
91 dead domain (D67E) and exposed for one hour to BMP2 (Fig. S1A). We then used mice carrying
92 floxed versions of *Dullard* allele and expressing the Cre recombinase under the *Pax3* or *Wnt1* loci,
93 which are active within the pre-delaminating cNCC (14,18,19), in combination with a ubiquitous
94 double-fluorescent Cre reporter allele, *Rosa26mTmG,* in which Cre-mediated recombination
95 labels all the NCC-derived cells with membrane-targeted GFP (mGFP+) (20). In agreement with
96 previous lineage analyses the pattern of cell recombination in the heart of embryos carrying
97 either Cre drivers matched that of the cNCC colonizing the cardiac cushions (Fig. S1B) (21,22). We
98 also confirmed by RT-qPCR that Fac-sorted (FACS) single GFP+ cells from *Wnt1*^{Cre}*; Dullard*$^{flox/flox}$*;*
99 *Rosa26mTmG* dissected hearts were recombined and did not express *Dullard* (Fig. S1C). We next
100 wanted to assess the activity of intracellular BMP signaling in the cNCC after *Dullard* deletion. To
101 this end, we immunolabelled the phosphorylated forms of Smad1/5/8, on serial cryosections
102 along the OFT axis in E11.5 embryos to follow the distal to proximal progression of cNCC (Fig. 1B,
103 C). Paralleling this time-dependent colonization, quantifications revealed variations of phospho-
104 Smad levels, which were more elevated proximally than distally (Fig. 1C). Furthermore, whatever
105 the levels along the OFT axis, there was a striking increase in Smads activity in both *Pax3*^{Cre} and

106 *Wnt1^{Cre}; Dullard$^{flox/flox}$* mutant cNCC compared to control cNCC (Fig. 1B, C). Altogether, these
107 results show that, although Dullard is not absolutely required for the establishment of a gradient
108 of BMP response in cNCC, it is necessary for a tight regulation of its magnitude.
109
110 **Dullard deletion in cNCC accelerates and jeopardizes OFT septation**
111
112 The absence of *Dullard* was embryonically lethal in both *Pax3^{Cre}* and *Wnt1^{Cre}* mice. While
113 *Pax3^{Cre}/Wnt1^{Cre}; Dullard$^{flox/flox}$* embryos were recovered at the expected 25% mendelian ratio by
114 E12.5, this ratio dropped below 10% afterward (Fig. S1D). We first assessed whether this could
115 be due to defects in cNCC colonization of the OFT. 3D imaging of GFP^{+} cNCC revealed that these
116 cells reached similar OFT levels in E11.5 control and *Dullard* mutants (Fig. S2A; Movie S1-S4). In
117 addition, no significant differences in the cNCC number nor in their proliferation and apoptosis
118 rates were detected between control and mutant OFT, although the mutant OFT tended to be
119 smaller in diameter (Fig. S2B-E). Thus, *Dullard* is not required for cNCC migration nor for their
120 amplification and survival in the OFT.
121
122 We next examined the heart septation status of *Dullard* mutants, knowing that cNCC are critical
123 in this morphogenesis process (4–6). For this, we monitored, using 3D lightsheet and confocal
124 microscopy, E11.5-12 hearts labelled for the arteries marker, Pecam (Fig. 2A; Movie S5, S6). At
125 distal levels, the OFT of control embryos displayed symmetrical septation and two great arteries
126 of similar size. In contrast, *Pax3^{Cre}/Wnt1^{Cre}; Dullard$^{flox/flox}$* embryos exhibited asymmetric
127 breakdown of the endocardium on the pulmonary side and obstruction of the pulmonary artery

128 (Pa) (Fig. 2A,B). At medial levels in *Pax3*^{Cre}/*Wnt1*^{Cre}; *Dullard*$^{flox/flox}$, the cardiac cushions were
129 already fused, though on the pulmonary side the Pa was absent compared to controls (Fig. 2B).
130 At medial levels in controls the endocardium attached to the presumptive pulmonary valve
131 intercalated-cushion (PV-IC), while in mutants this attachment had broken down and the
132 endocardium was pushed on the aortic side by converging cNCC. These observations
133 demonstrate that *Dullard* plays a pivotal role during cNCC-mediated OFT septation through the
134 modulation of BMP signalling and provided an explanation for the early lethality of *Dullard*
135 mutants, probably due to haemodynamics complications associated with Pa deficiency.
136

137 ***Dullard* controls cNCC mesenchymal state and Sema3c expression**
138

139 We set out to decipher the molecular basis of the defective OFT remodeling observed in
140 *Pax3*^{Cre}/*Wnt1*^{Cre}; *Dullard*$^{flox/flox}$ embryos. To address this question, we micro-dissected E11.5
141 *Wnt1*^{Cre}; *Dullard*$^{+/flox}$; *Rosa26mTmG* and *Wnt1*^{Cre}; *Dullard*$^{flox/flox}$; *Rosa26mTmG* OFT and sorted the
142 cNCC (GFP^{+}) and the endocardial cells (CD31^{+}) from the other OFT cell-types (RFP^{+}) (Fig. 3A). We
143 then performed single cell RT-qPCR for 44 genes implicated in epithelial-mesenchymal transition
144 (EMT), migration and/or specification of OFT progenitors (Table S1). Ct values extracted from the
145 Biomark chips were normalized using the mean value of *Actb* and *Gapdh* housekeeping genes
146 (Fig. S3A). We next performed an unsupervised hierarchical clustering of all cells according to
147 their molecular signature. This method allowed the segregation of 6 distinct OFT progenitor
148 subtypes (Fig. S3B): the Population 1 (Pop1) regrouped endocardial (CD31+) cells, all positive for
149 the endocardial markers, *Flt1*, *Kdr, Nfatc* and *Tek,* and the Pop5 encompassed epicardial cells

150 (*Tcf21* and *Wt1*). Importantly, these two populations contained cells derived from both *Wnt1*^{Cre}*;*
151 *Dullard*$^{+/flox}$ and *Wnt1*^{Cre}*; Dullard*$^{flox/flox}$ OFT. In contrast, the cNCC coming from *Wnt1*^{Cre}*;*
152 *Dullard*$^{+/flox}$ and *Wnt1*^{Cre}*; Dullard*$^{flox/flox}$ OFT were segregated in distinct subpopulations. The
153 control cNCC were mainly found in Pop2, while most mutant cNCC were in Pop4 and 6 (Fig. S3B).
154 This indicated that Dullard loss induced a drastic effect on the transcriptional state of cNCC, and
155 had little impact on the other progenitor cell-types.
156
157 We next decided to identify the transcriptomic changes underpinning the segregation between
158 mutant and control cNCC. By performing unsupervised hierarchical clustering only on cNCC, we
159 observed that the transcriptional state of cNCC was variable and that five populations of cells
160 could be defined (Pop1-5)(Fig 3B,C). Both control and mutant cNCC were found in Pop1 and 2,
161 and thus *Dullard* deletion did not impact the path between these transcriptional signatures (Fig.
162 S3C). Conversely, barely any mutant cNCC clustered with the Pop3 control cells. This population
163 of cells presented an upregulation of smooth muscle specification markers *Myh11* and *Acta2*,
164 indicating their commitment towards a smooth muscle fate, absent in mutant cNCC (Fig. 3D). In
165 contrast, mutant cNCC clustered in Pop4 and even more strongly in Pop5 (28% of mutant versus
166 3.95% of control cNCC) (Fig. S3C). Pop5 showed low levels of the mesenchymal markers *Snai2,*
167 *Twist1, Cdh2, Mmp14, Rac1* and high levels of the epithelial marker *Cdh5,* suggesting that mutant
168 cNCC transitioned towards epithelial-like states (Fig. 3D, Fig. S3B-E). In addition, this population
169 was characterized by higher levels of *Sema3c* expression, a chemokine implicated in cells
170 migration, and lower expression of its receptors *Nrp1* and *Plxnd1*. Cells in Pop4 resembled of
171 those in pop5, although the fold change in the levels of mesenchymal genes, *Cdh5* and *Sema3c*

172 compared to cNCC was less pronounced. This indicates a close relationship between these two
173 subsets which might represent two states of the differentiation path of *Dullard* mutated cNCC.
174 Similar analyses on the RFP$^+$ and CD31$^+$ cells did not show any major effect on RFP$^+$ cells, while
175 CD31$^+$ sorted from *Wnt1^{Cre}; Dullard$^{Flox/Flox}$* OFT presented a significant decrease in the expression
176 of *Twist1* and *Snai2* (Fig. S4A-D). In sum, our results suggest that *Dullard* deletion in cNCC mainly
177 affected cell-autonomously the NCC by changing their mesenchymal properties and their
178 communication properties via *Sema3c* signaling but had a very limited impact on the
179 transcriptional signature of the other OFT cell populations.
180

181 **_Sema3c_ expression is associated with cNCC condensation to the endocardium**
182 **and symmetrical differentiation of the SHF.**
183

184 We then investigated if the specific alterations in the transcriptome of *Wnt1^{Cre}; Dullard$^{flox/flox}$*
185 cNCC compared to control cells were translated into discrete traits in their behavior. First, by
186 using a nuclear staining, we analyzed at OFT lower levels, when the endocardium is not yet
187 ruptured, the condensation pattern of cNCC. In control embryos, sparse and elongated cNCC
188 nuclei were found at the proximity of the endocardium, whereas away from the endocardium
189 they harboured a rounded shape and high density (Fig. 4A; S5A). In mutant embryos, the sparse
190 population of cNCC was barely visible. We thus measured both the shortest distance between
191 cNCC nuclei and the endocardium as well as between each cNCC. *Wnt1^{Cre}; Dullard$^{flox/flox}$* cNCC
192 presented a significant decrease both in distance to the endocardium and to their closest
193 neighbor compared to the *Wnt1^{Cre}; Dullard$^{+/flox}$* cNCC (Fig. 4B). Hence, in absence of *Dullard,* cNCC

194 are more aggregated and closer to the endocardium than controls (Fig 4A), in coherence with the
195 the transcriptional transition towards epithelial-like states (Fig. 3). In addition, we noticed that
196 the orientation of the cNCC nuclei relative to the endocardium, revealing cell orientation, was
197 different between control and mutant OFT. We consequently determined the angle formed by
198 the longest axis of the different cNCC with the axis spanning the endocardium and plotted it in a
199 [0°,90°] referential. While in control embryos, most cNCC nuclei were parallel to the
200 endocardium, in *Dullard* mutants a significantly higher percentage of cNCC presented nuclei
201 standing perpendicular to the endocardium (Fig. S5B). In absence of *Dullard*, the aggregation of
202 cNCC, their convergence towards the endocardium and orientation relative to the endocardium
203 are enhanced compared to control cells demonstrating that *Dullard* regulates cNCC
204 morphogenetic cellular properties involved in OFT septation.
205
206 *Sema3c* stands as a cue involved in cNCC convergence towards the endocardium (6), and was
207 upregulated in our single cell transcriptional studies. We analyzed its distribution at the mRNA
208 level by *in situ* hybridization (ISH) performed on OFT serial sections and confirmed the increase
209 in *Sema3c* expression in Pax3/*Wnt1*^{Cre};*Dullard*$^{flox/flox}$ cNCC (Fig. 4C, S5C). The *Sema3c* expression
210 territories increased distally forming a gradient along the OFT axis of both control and mutant
211 embryos, parallel to the previously described gradient of BMP signaling activity. Moreover, in the
212 distal region, *Sema3c* expression territories converged towards the endocardium and thus
213 associated with areas of cNCC condensation (Fig. 4A,C; S5A,C). Hence, our results highlight a
214 BMP-regulated gradient of *Sema3c e*xpression, established along the OFT by the cNCC, that drives

215 the zipper-like convergence of the cNCC towards the endocardium, and the distal to proximal
216 OFT septation.
217
218 At the distal OFT level, the outer SHF is differentiating in myocardium and starts to express
219 Myosin Heavy Chain (MyHC, stained by MF20 antibody) (Fig 4D) (23,24). First, we noted a
220 coregionalization of SHF progenitors expressing MyHC and Sema3c, which is a marker of
221 subpulmonary myocardium (compare Fig. 4C and Fig. S5C with Fig. S5D) (25,26). Second, the
222 MyHC myocardium localization differed between *Pax3*^{Cre}*/Wnt1*^{Cre}*;Dullard*$^{flox/flox}$ and
223 *Pax3*^{Cre}*/Wnt1*^{Cre}*;Dullard*$^{flox/+}$ embryos. In the later, the MyHC+ myocardium was located medially
224 and symmetrically between the Ao and Pa sides, whereas in the former it was asymmetrically
225 positioned on the pulmonary side (Fig 4D, Fig. S5D). These observations highlight that
226 symmetrical septation at the distal OFT level is supported by the medial differentiation of
227 subpulmonary myocardium and that the BMP-dependent regulation of *Sema3c* expression in the
228 cNCC is crucial for symmetrical positioning of the differentiating subpulmonary myocardium.
229
230

231 **Discussion**
232

233 By looking into the function of the *Dullard* phosphatase during cNCC-mediated OFT septation, we
234 have uncovered that spatially regulated BMP-dependent aggregation of cNCC set the timing and
235 symmetrical shaping of the endocardium rupture. We showed that a gradient of BMP activation
236 exists in the cNCC along the OFT axis, and notably its amplitude, is under the control of the

237 phosphatase *Dullard*. Other mechanisms are likely to be responsible for its decline along the OFT,
238 as it is still observed in absence of *Dullard*. In contrast to other developmental systems, this
239 spatial gradient of BMP activity is unlikely resulting from a gradient of ligand diffusing from a
240 localized distal source (27). BMP4, particularly, is homogeneously expressed in the myocardium
241 throughout the entire length of the OFT (8,9,11,28,29). Instead, intracellular signalling inhibitors
242 could allow a temporal adaptation of cNCC to BMP signals during their proximal ingression.
243 Prominent expression of *Smad6*, a BMP negative feedback effector, or of the diffusible inhibitor
244 *Noggin* is observed in the OFT from E10.5 throughout great arteries formation (30,31).
245
246 Importantly, this gradient provides a means by which the zipper-like septation of the OFT can
247 proceed. The levels of BMP stand as a sufficient parameter to tune the degree of convergence
248 and aggregation of cNCC to the endocardium. As such, lowering down BMP levels prevents the
249 expansion of the cardiac cushions and leads to persistent truncus arteriosus (11,12), while
250 increasing BMP signalling triggers premature cNCC condensation to the endocardium and
251 accentuated OFT septation (Fig 2). This model is further supported by evidence showing that
252 altering the ability of cNCC to contract, migrate and adhere, hence to condensate, prevents the
253 correct formation and positioning of the aorticopulmonary septum (5,6,32).
254
255 We have uncovered part of the molecular mechanisms by which BMP controls cNCC behavior. A
256 BMP over-activation triggers a downregulation of mesenchymal markers, reminiscent of a
257 transition of the cNCC towards epithelial-like states, with a loss of migratory freedom and
258 increased cohesiveness between cells (33). Furthermore, out of the transcriptional changes

259 induced by *Dullard* loss, several lines of evidence support the idea that the up-regulation of
260 *Sema3c* is likely to play a predominant role in the increased compaction of cNCC. The secretion
261 of this guiding cue from the subpulmonary myocardium attracts cNCC towards the OFT, while its
262 expression in the cNCC is required for their convergence to the endocardium (6,34,35). *Sema3c*
263 is also promoting the self aggregation of cNCC, as demonstrated in primary cultures (36). Besides,
264 our results show that increased *Sema3c* levels precipitate OFT septation, not by breaking the
265 endocardium structure itself as expected by previously shown involvement of *Sema3c* in the NCC
266 during the endocardium EMT (Plein et al., 2015), but through a rupture in the attachment of the
267 endocardium to the subpulmonary wall. Finally, our observations indicate that the correct
268 septation onset, at the distal OFT level, requires the central positioning of differentiating
269 subpulmonary myocardium. BMP mediated induction of *Sema3c* would control the isotropic
270 localization of differentiated myocardial cells. On an evolutionary perspective, Keyte et al.
271 postulated that the emergence of *Sema3c* expression in the pulmonary myocardium has
272 represented a turning point in the dialogue between SHF and cNCC by attracting cNCC to the
273 OFT (37). Our results suggest that conversely, cNCC have a favored ability to dialogue with the
274 subpulmonary myocardium, consolidating the idea of a co-evolution between the cNCC and
275 subpulmonary myocardium during the evolution of the pulmonary circulation.
276
277

278 **Experimental procedures**

279

280 *Mouse strains*

281 All animal experiments were approved by the Animal Ethics Committee of Sorbonne University.
282 We used the mouse strains described in the following papers with their MGI IDs: *Dullard*$^{flox/flox}$
283 Acc No. CDB0564K, Web site : http://www.cdb.riken.jp/arg/mutant%20mice%20list.html
284 (Sakaguchi et al. 2013), *Pax3*^{Cre} ((19), MGI: 3573783), *Wnt1*^{Cre} ((18), MGI:2386570),
285 *Rosa26mTmG* ((20), MGI: 3716464), and *C57BL/6JRj* (Janvier Labs).

286

287 *Immunohistochemistry and imaging*

288 Mouse embryos were collected at E11.5 and dissected in PBS (4°c), incubated 5min in 200mM
289 KCl to stop heart beating and fixed for 2-3 hours in 4% PFA (Electron Microscopy Science,
290 #15710S) at 4°c. They were cryoprotected in 20% sucrose overnight at 4°c, embedded in OCT,
291 and cryosectioned at 12µm thickness.
292 Sections were permeabilized 10min in PBS/0.5% Triton, incubated for 1h in blocking buffer (5%
293 goat serum in PBS) and overnight in primary antibody solution (in 1% BSA in PBS). After thorough
294 washing they were incubated 1h in secondary antibody solution (in 1% BSA in PBS). Lightsheet
295 acquisition was performed on whole embryos cleared following the 3Disco protocol,
296 immunostained and imaged using an ultramicroscope (LaVision BioTec) (38). 3D confocal
297 microscopy was performed on micro-dissected OFT regions immunostained, clarified with BABB
298 and acquired using a LSM700 confocal microscope (Carl Zeiss) (39). 3D renderings were
299 generated using the Imaris software.

300

301 The primary antibodies used on cryosections include the following: GFP (chicken, Aves Labs, GFP-
302 1020, 1/500), Pecam (rat monoclonal, Santa-Cruz Biotechnology, sc-18916, 1/200), Phospho-
303 Smad1/5/8 (rabbit monoclonal, Cell Signaling Technology,13820S,1/500), myosin heavy chain,
304 MyHC (mouse monoclonal, DSHB, MF20,1/300), Smooth Muscle Actin (mouse monoclonal,
305 Sigma-Aldrich, A2547, 1/300), Phospho-Histone H3 (rabbit, Cell Signaling Technology, 9701,
306 1/500), Cleaved Caspase-3 (rabbit monoclonal, Cell Signaling Technology, Asp175, 1/500).
307

308 *In situ hybridisation*

309 The Sema3c probe was provided by the lab of S. Zaffran (25). Cryosections were processed
310 following the protocol described in (40).
311

312 *Image analysis and quantification*

313 Immunostainings were acquired using a Nikon Ti2 microscope and Metamorph (Molecular
314 Devices), then assembled and analyzed on Fiji (41). Quantification of P-Smad1/5/8 was
315 performed in cNCC by using the GFP channel as a mask. Measures of cNCC distance and
316 orientation to the endocardium were performed using Metamorph (Molecular Devices). The
317 coordinates of the endocardium extremities were registered to create a reference axis as well all
318 cNCC nuclei longest axis coordinates. From these data we inferred the centroid coordinates of all
319 cNCC nuclei and calculated their distances and angles to the endocardium axis.
320

321 *Cell culture and transfection*

322 C2C12 cells were cultivated at 37°C/5% CO2, in growth medium (DMEM, 4.5g/L, D-glucose, 4mM
323 L-glutamine, 1mM sodium pyruvate, 10% fetal calf serum). Plasmid transfection was performed
324 using Lipofectamine 2000 (Life Technologies). 24 hours after transfection, BMP2 recombinant
325 human protein (Thermo Fisher Scientific, #PHC7145) was applied for 1h on cells. Cells were fixed
326 with 4% PFA and immunostained with the phospho-Smad1/5/8 antibody. Or, cells were washed
327 in PBS, collected with PBS 1% SDS and passed through Qiashredder columns (Qiagen) to disrupt
328 nucleic acids. Proteins extracts were then processed for Western blotting using pre-cast gels (Life
329 Technologies) and transferred on nitrocellulose by semi-dry transfer (Bio-Rad).

330

331

332 *Tissue dissociation and FACS sorting*

333 Mouse embryos were collected at E11.5 and placed in HBSS/1% FBS (HBSS +/+, Invitrogen) during
334 genotyping. OFT were micro-dissected and dissociated by 15min incubation in collagenase
335 (0.1mg/ml in H_2O, C2139 Sigma) and thorough pipetting. HBSS (10% FBS) was added to the cells
336 medium to stop the enzymatic reaction. OFT cell suspensions were centrifuged and resuspended
337 in HBSS (1% FBS) before immunostaining. The panel of conjugated antibodies used for FACS
338 included Ter119 Pe-Cy7 (Erythroid Cells, anti-mouse, Sony, Catalog No. 1181110, 1/300), CD45
339 APC-Cy7 (Rat anti-mouse, BD Pharmingen, Catalog No. 557659, 1/300), CD31 APC (Rat anti-
340 mouse, BD Pharmingen, Clone MEC 13.3 Catalog No. 561814, 1/300) diluted in HBSS (1% FBS).
341 Cells were centrifuged and resuspended in the antibody solution for a 25min incubation period
342 (4°C, dark), washed several times, filtered (Fisher cell strainer, 70µm mesh) and 7AAD PE-Cy7
343 (1/800) was added in the cells suspension to exclude dead cells. Cells were sorted in a BD
344 FACSAria™ III into 96-well plates loaded with RT-STA reaction mix (CellsDirect™ One-Step qRTPCR
345 Kit, Invitrogen) and 0.2x specific TaqMan ® Assay mix (see Table 1 for assays list).

346

347 *Single-Cell gene expression*

348 Sorted cells in RT-STA reaction mix from the CellsDirect TM One-Step qRT-PCR Kit (Life
349 Technologies), reverse transcribed and specific target pre-amplified (20 cycles), according to the
350 manufacturer's procedures. Pre-amplified samples were diluted 5x with low EDTA TE buffer prior
351 to qPCR analysis using 48.48 Dynamic Array TM IFCs and the BioMark TM HD System (Fluidigm).
352 The same TaqMan® gene expression assays (20x, Life Technologies) were individually diluted 1:1

353 with 2x assay loading reagent (Fluidigm). Pre-amplified samples were combined with TaqMan
354 Universal Master Mix (Life Technologies) and 20x GE sample loading reagent (Fluidigm). Loading
355 of the 48.48 Dynamic Array TM IFCs and qPCR cycling conditions followed the Fluidigm procedure
356 for TaqMan ® gene expression assays.
357

358 *Bioinformatic analysis*

359 The analytic framework used followed the one described in (42). For visualisation of the single
360 cell multiplex qPCR, done on 44 genes, we generated a heatmap using the pHeatmap (v1.0.10) R
361 package (v3.2.2).
362

363 *Statistical analysis*

364 Statistical analysis was performed with the Student's t-test or Mann-Whitney test depending on
365 normality. The analysis was performed using Prism Software (GraphPad). Statistical significance
366 is represented as follows: ***$p < 0.001$. All results are shown as mean ± standard deviation.
367

Acknowledgments

We thank the Cadot, Bitoun and Ribes Laboratories for discussions, Sigolène Meilhac for her help on understanding heart development concepts, Edgar Gomes laboratories for useful comments, Stéphane Zaffran for the *Sema3c* ISH probe and Morgane Belle for Lightsheet microscopy. The *Pax3*^{Cre} and *Rosa26mTmG* transgenic lines were kindly provided by F. Relaix, and the *Wnt1*^{Cre} line by A. Pierani. This work was supported by Agence Nationale pour la Recherche (ANR-14-CE09-0006-04) to BC; Association Institut de Myologie to BC. V.R. is an INSERM researcher, and work in her lab is supported by CNRS/INSERM ATIP-AVENIR program, as well as by a Ligue Nationale Contre le Cancer grant (PREAC2016.LCC). MV has a postdoctoral fellowship from the Laboratoire d'Excellence Revive (Investissement d'Avenir; ANR-10-LABX-73).

Authors contributions

JFD, PM, GC, MV and BC performed the experiments; MP analyzed the transcriptomics data; JFD, VR and BC conceived and designed the experiments; JFD, VR and BC wrote the manuscript with assistance from MV and GC; DSO and RN provided reagents.

387 # Figures legends

388

389 **Figure 1: Dullard is required to downregulate cNCC response to myocardial BMP signals. A**: On
390 the left, schematic representation of cNCC (green) migrating from the neural tube, through the
391 somites (S) 1 to 3, towards the heart region (red). On the right, schematic transversal sections of
392 the OFT showing cardiac cushions colonization by cNCC supporting OFT septation. **B:** Transversal
393 sections of E11.5 control *Wnt1^{Cre}/Pax3^{Cre}; Dullard$^{flox/+}$*; *Rosa26mTmG* and mutant
394 *Wnt1^{Cre}/Pax3^{Cre}; Dullard$^{flox/flox}$*; *Rosa26mTmG* hearts labelled for phospho-Smad1/5/8
395 (PSmad1/5/8) and cNCC-derived GFP+ (green). Green dotted lines delineate the cNCC. **C:** Heart
396 schema displaying the position along the OFT distal-proximal axis of transverse sections used to
397 measure PSmad1/5/8 levels and graph showing PSmad1/5/8 intensity levels in the cNCC
398 (mean+/-s.e.m.)

399

400 **Figure 2: Dullard deletion in cNCC causes asymmetric and premature OFT septation. A.** Three-
401 dimensional rendering of the OFT from E11.5 *Pax3^{Cre}; Dullard$^{flox/+}$* and *Pax3^{Cre}; Dullard$^{flox/flox}$*
402 embryos (Pa width represented with an oblique white line). **B.** Transversal sections along the OFT
403 of E11.5 *Wnt1^{Cre}; Dullard$^{flox/+}$*; *Rosa26mTmG* and mutant *Wnt1^{Cre}; Dullard$^{flox/flox}$*; *Rosa26mTmG*
404 embryos stained for Pecam (red) and GFP (green). Brackets highlight the asymmetry between the
405 Ao and Pa poles in mutants compared to controls. Arrowheads point at the ruptured
406 endocardium in mutant embryos contrasting with its unruptured state in controls. Ao: Aorta; Pa:
407 pulmonary artery; PV-IC: Pulmonary valve intercalated-cushion

408

409 **Figure 3: Single-cell analyses unravel a role for Dullard in regulating transcriptomic states of**
410 **cNCC. A:** Main steps performed to profile gene expression in OFT progenitor cells sorted from
411 *Wnt1^{Cre}; Dullard$^{flox/+}$*; *Rosa26mTmG* and *Wnt1^{Cre}; Dullard$^{flox/flox}$*; *Rosa26mTmG* E11.5 embryos. **B:**
412 Unsupervised hierarchical clustering of GFP^{+} cNCC based on the levels of expression of the 44
413 genes included in the panel (Table S1). **C:** Diffusion maps of the cNCC according to their cluster
414 of appartenance and their genotype. **D:** Boxplot representation of the expression level of genes
415 differentially expressed between cNCC Pop3 and 5.
416
417 **Figure 4: BMP signaling regulates *Sema3c* expression and cNCC condensation, as well as distal**
418 **myocardialization**. **A:** Transversal sections of the OFT stained with DAPI. The endocardium is
419 delineated with a red line and the inner side of the myocardium with a greyline. Areas where
420 cNCC are of high density and rounded nuclear shape are surrounded with a green dotted line,
421 while areas where cNCC are of low density and elongated nuclear shape are surrounded with a
422 yellow dotted line. **B:** Measure of the shortest distance between cNCC nuclei and to the
423 endocardium in both genotypes (5 embryos analyzed per genotype, Mann-Whitney Test, P-value
424 < 0.0001). **C:** Sema3c ISH and Pecam/GFP immunostaining on OFT transversal sections at distal,
425 medial and proximal levels, from the indicated genotypes. **D:** Distal sections of the OFT stained
426 for Myosin Heavy Chain (MF20) to mark differentiated myocardium in control and mutant
427 embryos.
428
429
430

431 **Figure S1: Dullard is a regulator of BMP signaling and its deletion in Neural Crest Cells induces**
432 **embryonic death around E12.5. A:** Top: Western blot of the phosphorylation of Smad1/5/8 in
433 the muscle cell line C2C12 after exposure to BMP2 for 1H. Cells transfected with Dullard (Dull)
434 do not show any phosphorylation of Smad1/5/8 whereas a mutation in the phosphatase domain
435 (D67E) retains this phosphorylation. Bottom-left: A similar result was obtained by
436 immunofluorescence showing that only cells transfected with Dullard do not have nuclear
437 phosphorylated Smad1/5/8. Right: A quantification of three different experiments was
438 performed on transfected cells. **B:** *Wnt1*^{Cre} and *Pax3*^{Cre} mouse driver lines present the same
439 pattern of cNCC colonization in the OFT as shown by the reporter line *Rosa26mTmG* . **C:** Results
440 of the RT-qPCR on single cells from the OFT showing that only the GFP+ cNCC were effectively
441 depleted of Dullard. Few RFP+ cells present a down regulation of Dullard, probably due to an
442 ineffective recombination of the *Rosa26mTmG* reporter (but not of the Dullard floxed allele) by
443 the Cre driver. **D:** Percentage of living *Pax3*^{Cre}*/Wnt1*^{Cre}*; Dullard*$^{flox/flox}$ embryos before and after
444 E12.5 (percentage calculated on 25 *Pax3*^{Cre} and 40 *Wnt1*^{Cre} litters recovered at embryonic stages
445 spanning embryonic gestation).
446
447 **Figure S2: Absence of Dullard in cNCC does not affect their colonization and survival in the OFT.**
448 **A:** Left: Three dimensional rendering of cNCC (green) over Pecam (white) after BABB clearing and
449 confocal acquisition of *Wnt1*^{Cre}; *Dullard*$^{flox/+}$; *Rosa26mTmG* and *Wnt1*^{Cre}; *Dullard*$^{flox/flox}$;
450 *Rosa26mTmG* E11.5 embryos. Right: Three dimensional rendering of cNCC (green isosurface)
451 over Pecam (white) after 3Disco clearing and Lightsheet acquisition of *Pax3*^{Cre}; *Dullard*$^{flox/+}$;
452 *Rosa26mTmG* and *Pax3*^{Cre}; *Dullard*$^{flox/flox}$; *Rosa26mTmG* E12 embryos. No defect in the

453 colonization of the cNCC in the OFT was observed. **B, C, D:** Quantification of cNCC total number
454 per section of OFT, proliferative cNCC through PH3 staining and apoptotic cNCC through cleaved-
455 caspase-3 staining. We do not observe any significant difference between genotypes. **E:**
456 Representation of the OFT and the different levels of sectioning. Quantification of the OFT
457 transversal area along its proximal-distal axis, which shows a slight reduction in E11.5 *Wnt1*^{Cre};
458 *Dullard*$^{flox/flox}$OFT compared to controls.
459
460 **Figure S3: Single-cell transcriptional analyses of OFT progenitors at E11.5. A:** Graph showing the
461 linear regression between *Actb* and *Gapdh* Ct values. **B:** Unsupervised clustering heatmap of the
462 OFT progenitors from *Wnt1*^{Cre}*; Dullard*$^{+/flox}$*; Rosa26mTmG* and *Wnt1*^{Cre}*; Dullard*$^{flox/flox}$*;*
463 *Rosa26mTmG* based on the gene expression level of the 44 genes included in the panel (Table
464 S1). Six different populations can be discriminated, among which the endocardial (Pop1)
465 progenitors expressing high levels of *Flt1*, *Kdr*, *Nfatc1* and *Tek*, and the pericardial (Pop5)
466 progenitors expressing high levels of *Wt1*, *Tcf21.* **C:** Statistical distribution of *Wnt1*^{Cre}*; Dullard*$^{+/flox}$*;*
467 *Rosa26mTmG* and *Wnt1*^{Cre}*; Dullard*$^{flox/flox}$*; Rosa26mTmG* cNCC in the 5 cNCC clusters defined by
468 their distinct transcriptional signatures. **D:** Genetic composition of the diffusion components (DC)
469 1 and 2, on which are based the diffusion maps presented in Fig. 3C. **E:** Expression levels of genes
470 highlighted in DC1 and 2 and not presented in Fig. 3D.
471
472 **Figure S4: Analysis of the transcriptional signatures of control and mutant RFP+ CD31- and RFP+**
473 **CD31+ (endocardial) progenitors. A:** Left: Unsupervised clustering heatmap of the RFP+ CD31-
474 progenitors from *Wnt1*^{Cre}*; Dullard*$^{+/flox}$*; Rosa26mTmG* and *Wnt1*^{Cre}*; Dullard*$^{flox/flox}$*;*

475 *Rosa26mTmG* based on the gene expression level of the 44 genes included in the panel (Table
476 S1). Five different populations can be discriminated, all composed of both control and mutant
477 RFP+ CD31+ cells. Right: Unsupervised clustering heatmap of the RFP+ CD31+ (endocardial)
478 progenitors. Six populations with distinct transcriptional signatures (Pop1-6) emerged from the
479 clustering, and Pop1 and 6 presented clear segregation of control and mutant endocardial cells.
480 **B:** Diffusion maps of the endocardial progenitors according to their cluster of appartenance and
481 their genotype, and based on the diffusion components (DC) 1 and 2 presented in C. **C:** Genetic
482 composition of DC 1 and 2, on which are based the diffusion maps presented in B. **D:** Expression
483 levels of genes highlighted in DC1 and 2.
484
485 **Figure S5: BMP signaling regulates *Sema3c* expression, cNCC compaction and orientation, as**
486 **well as distal myocardialization. A:** Transversal sections of *Pax3*^{Cre}*; Dullard*$^{flox/flox}$ and *Pax3*^{Cre}*;*
487 *Dullard*$^{+/flox}$ OFT stained with DAPI. The endocardium is delineated with a red line and the inner
488 side of the myocardium with a greyline. Areas where cNCC are of high density and rounded
489 nuclear shape are surrounded with a green dotted line, while areas where cNCC are of low
490 density and elongated nuclear shape are surrounded with a yellow dotted line. In *Wnt1*^{Cre}*;*
491 *Dullard*$^{flox/flox}$ mutants, the region of high cNCC density is closer to the endocardium compared to
492 controls. **B:** Left: Measure, in *Wnt1*^{Cre}*; Dullard*$^{flox/flox}$ and *Wnt1*^{Cre}*; Dullard*$^{+/flox}$ cardiac cushions, of
493 the angles formed by cNCC nuclei longest axis with the endocardial axis, plotted in a [0;90°]
494 referential. Right: Mapping of the cNCC in the cushions of representative control and mutant
495 embryos, color-coded according to their angle to the endocardium. Dark blue represents angles
496 parallel to the endocardium, while dark red are perpendicular. 5 embryos were analyzed for both

497 genotypes. **C:** Sema3c ISH and Pecam/GFP immunostaining on OFT transversal sections at distal,
498 medial and proximal levels, from the indicated genotypes. The areas of *Sema3c* expression
499 (delineated in green) are highly increased in the *Pax3*^{Cre}*; Dullard*$^{flox/flox}$ embryos compared to
500 controls. These areas are bigger and closer to the endocardium (delineated in red) at distal levels
501 in both genotypes, and highest *Sema3c* expression correlates with endocardial breakdown. **D:**
502 Distal sections of the OFT stained for Myosin Heavy Chain (MF20) show an asymmetric
503 localization of differentiated myocardium in *Wnt1*^{Cre}*; Dullard*$^{flox/flox}$ embryos. The differentiating
504 MF20+ myocardium is located in Sema3c+ areas of the myocardium (compare Fig. 4C and Fig.
505 S5D), which indicates that it belongs to the subpulmonary lineage.
506
507 **Movie S1/S2:** Three dimensional rendering of cNCC (green) over Pecam (white) after BABB
508 clearing and confocal acquisition of *Wnt1*^{Cre}; *Dullard*$^{flox/+}$*; Rosa26mTmG* and *Wnt1*^{Cre};
509 *Dullard*$^{flox/flox}$*; Rosa26mTmG* E11.5 embryos. No defect in the OFT colonization of mutant cNCC is
510 observed.
511
512 **Movie S3/S4:** Three dimensional rendering of cNCC (green isosurface) over Pecam (white) after
513 3Disco clearing and Lightsheet acquisition of *Pax3*^{Cre}; *Dullard*$^{flox/+}$*; Rosa26mTmG* and *Pax3*^{Cre};
514 *Dullard*$^{flox/flox}$*; Rosa26mTmG* E12 embryos. No defect in the OFT colonization of mutant cNCC is
515 observed.
516
517 **Movie S5/S6:** Three dimensional rendering of cNCC (green isosurface) over Pecam (red
518 isosurface) after 3Disco clearing and Lightsheet acquisition of *Pax3*^{Cre}; *Dullard*$^{flox/+}$*; Rosa26mTmG*

519 and *Pax3*^{Cre}; *Dullard*$^{flox/flox}$; *Rosa26mTmG* E12 embryos. An atrophy of the pulmonary artery is

520 observed.

521

522 **Table S1:** List of TaqMan® gene expression assays (20x, Life Technologies) used for single-cell

523 qPCRs experiments.

524
525

526 # References

527

528 1. Brickner ME, Hillis LD, Lange RA. Congenital heart disease in adults. First of two parts. N Engl J Med.
529 2000 Jan 27;342(4):256–63.

530 2. Kelly RG. Chapter two - The Second Heart Field. In: Bruneau BG, editor. Current Topics in
531 Developmental Biology [Internet]. Academic Press; 2012 [cited 2018 Jul 6]. p. 33–65. (Heart
532 Development; vol. 100). Available from:
533 http://www.sciencedirect.com/science/article/pii/B9780123877864000026

534 3. Keyte A, Hutson MR. The Neural Crest in Cardiac Congenital Anomalies. Differ Res Biol Divers. 2012
535 Jul;84(1):25–40.

536 4. Bockman DE, Redmond ME, Waldo K, Davis H, Kirby ML. Effect of neural crest ablation on
537 development of the heart and arch arteries in the chick. Am J Anat. 1987 Dec;180(4):332–41.

538 5. Phillips HM, Mahendran P, Singh E, Anderson RH, Chaudhry B, Henderson DJ. Neural crest cells are
539 required for correct positioning of the developing outflow cushions and pattern the arterial valve
540 leaflets. Cardiovasc Res. 2013 Aug 1;99(3):452–60.

541 6. Plein A, Calmont A, Fantin A, Denti L, Anderson NA, Scambler PJ, et al. Neural crest–derived SEMA3C
542 activates endothelial NRP1 for cardiac outflow tract septation. J Clin Invest. 2015 Jul 1;125(7):2661–
543 76.

544 7. Waldo K, Miyagawa-Tomita S, Kumiski D, Kirby ML. Cardiac Neural Crest Cells Provide New Insight
545 into Septation of the Cardiac Outflow Tract: Aortic Sac to Ventricular Septal Closure. Dev Biol. 1998
546 Apr 15;196(2):129–44.

547 8. Jiao K, Kulessa H, Tompkins K, Zhou Y, Batts L, Baldwin HS, et al. An essential role of Bmp4 in the
548 atrioventricular septation of the mouse heart. Genes Dev. 2003 Oct 1;17(19):2362–7.

549 9. Liu W, Selever J, Wang D, Lu M-F, Moses KA, Schwartz RJ, et al. Bmp4 signaling is required for
550 outflow-tract septation and branchial-arch artery remodeling. Proc Natl Acad Sci U S A. 2004 Mar
551 30;101(13):4489–94.

552 10. McCulley DJ, Kang J-O, Martin JF, Black BL. BMP4 is required in the anterior heart field and its
553 derivatives for endocardial cushion remodeling, outflow tract septation, and semilunar valve
554 development. Dev Dyn. 2008 Nov 1;237(11):3200–9.

555 11. Jia Q, McDill BW, Li S-Z, Deng C, Chang C-P, Chen F. Smad signaling in the neural crest regulates
556 cardiac outflow tract remodeling through cell autonomous and non-cell autonomous effects. Dev
557 Biol. 2007 Nov 1;311(1):172–84.

558 12. Stottmann RW, Choi M, Mishina Y, Meyers EN, Klingensmith J. BMP receptor IA is required in
559 mammalian neural crest cells for development of the cardiac outflow tract and ventricular
560 myocardium. Dev Camb Engl. 2004 May;131(9):2205–18.

561 13. Tang S, Snider P, Firulli AB, Conway SJ. Trigenic neural crest-restricted Smad7 over-expression results
562 in congenital craniofacial and cardiovascular defects. Dev Biol. 2010 Aug 1;344(1):233–47.

563 14. Sakaguchi M, Sharmin S, Taguchi A, Ohmori T, Fujimura S, Abe T, et al. The phosphatase Dullard
564 negatively regulates BMP signalling and is essential for nephron maintenance after birth. Nat
565 Commun. 2013 Jan 29;4:1398.

566 15. Satow R, Kurisaki A, Chan T, Hamazaki TS, Asashima M. Dullard Promotes Degradation and
567 Dephosphorylation of BMP Receptors and Is Required for Neural Induction. Dev Cell. 2006
568 Dec;11(6):763–74.

569 16. Urrutia H, Aleman A, Eivers E. Drosophila Dullard functions as a Mad phosphatase to terminate BMP
570 signaling. Sci Rep. 2016 Aug 31;6:32269.

571 17. Bruce DL, Sapkota GP. Phosphatases in SMAD regulation. FEBS Lett. 2012 Jul 4;586(14):1897–905.

572 18. Danielian PS, Muccino D, Rowitch DH, Michael SK, McMahon AP. Modification of gene activity in
573 mouse embryos in utero by a tamoxifen-inducible form of Cre recombinase. Curr Biol. 1998 Dec
574 3;8(24):S1–2.

575 19. Engleka KA, Gitler AD, Zhang M, Zhou DD, High FA, Epstein JA. Insertion of Cre into the Pax3 locus
576 creates a new allele of Splotch and identifies unexpected Pax3 derivatives. Dev Biol. 2005 Apr
577 15;280(2):396–406.

578 20. Muzumdar MD, Tasic B, Miyamichi K, Li L, Luo L. A global double-fluorescent Cre reporter mouse.
579 genesis. 2007 Sep 1;45(9):593–605.

580 21. Brown CB, Feiner L, Lu M-M, Li J, Ma X, Webber AL, et al. PlexinA2 and semaphorin signaling during
581 cardiac neural crest development. Development. 2001 Aug 15;128(16):3071–80.

582 22. Jiang X, Rowitch DH, Soriano P, McMahon AP, Sucov HM. Fate of the mammalian cardiac neural
583 crest. Development. 2000 Apr 15;127(8):1607–16.

584 23. van den Hoff MJB, Moorman AFM, Ruijter JM, Lamers WH, Bennington RW, Markwald RR, et al.
585 Myocardialization of the Cardiac Outflow Tract. Dev Biol. 1999 Aug 15;212(2):477–90.

586 24. Phillips HM, Murdoch JN, Chaudhry B, Copp AJ, Henderson DJ. Vangl2 Acts via RhoA Signaling to
587 Regulate Polarized Cell Movements During Development of the Proximal Outflow Tract. Circ Res.
588 2005 Feb 18;96(3):292–9.

589 25. Bajolle F, Zaffran S, Kelly RG, Hadchouel J, Bonnet D, Brown NA, et al. Rotation of the Myocardial
590 Wall of the Outflow Tract Is Implicated in the Normal Positioning of the Great Arteries. Circ Res
591 [Internet]. 2006 Feb 17 [cited 2018 Sep 21]; Available from:
592 https://www.ahajournals.org/doi/abs/10.1161/01.RES.0000202800.85341.6e?url_ver=Z39.88-
593 2003&rfr_id=ori:rid:crossref.org&rfr_dat=cr_pub%3dpubmed

594 26. Rana MS, Théveniau-Ruissy M, Bono CD, Mesbah K, Francou A, Rammah M, et al. Tbx1 Coordinates
595 Addition of Posterior Second Heart Field Progenitor Cells to the Arterial and Venous Poles of the
596 HeartNovelty and Significance. Circ Res. 2014 Oct 10;115(9):790–9.

597 27. Bier E, De Robertis EM. BMP gradients: A paradigm for morphogen-mediated developmental
598 patterning. Science. 2015 Jun 26;348(6242):aaa5838–aaa5838.

599 28. Jones CM, Lyons KM, Hogan BL. Involvement of Bone Morphogenetic Protein-4 (BMP-4) and Vgr-1
600 in morphogenesis and neurogenesis in the mouse. Development. 1991 Feb 1;111(2):531–42.

601 29. Zhang J, Chang JYF, Huang Y, Lin X, Luo Y, Schwartz RJ, et al. The FGF-BMP Signaling Axis Regulates
602 Outflow Tract Valve Primordium Formation by Promoting Cushion Neural Crest Cell
603 DifferentiationNovelty and Significance. Circ Res. 2010 Nov 12;107(10):1209–19.

604 30. Choi M, Stottmann RW, Yang Y-P, Meyers EN, Klingensmith J. The Bone Morphogenetic Protein
605 Antagonist Noggin Regulates Mammalian Cardiac Morphogenesis. Circ Res. 2007 Feb 2;100(2):220–
606 8.

607 31. Galvin KM, Donovan MJ, Lynch CA, Meyer RI, Paul RJ, Lorenz JN, et al. A role for Smad6 in
608 development and homeostasis of the cardiovascular system. Nat Genet. 2000 Feb;24(2):171–4.

609 32. Luo Y, High FA, Epstein JA, Radice GL. N-cadherin is required for neural crest remodeling of the
610 cardiac outflow tract. Dev Biol. 2006 Nov 15;299(2):517–28.

611 33. Kim HY, Jackson TR, Davidson LA. On the role of mechanics in driving mesenchymal-to-epithelial
612 transitions. Semin Cell Dev Biol. 2017 Jul 1;67:113–22.

613 34. Feiner L, Webber AL, Brown CB, Lu MM, Jia L, Feinstein P, et al. Targeted disruption of semaphorin
614 3C leads to persistent truncus arteriosus and aortic arch interruption. Development. 2001 Aug
615 15;128(16):3061–70.

616 35. Toyofuku T, Yoshida J, Sugimoto T, Yamamoto M, Makino N, Takamatsu H, et al. Repulsive and
617 attractive semaphorins cooperate to direct the navigation of cardiac neural crest cells. Dev Biol.
618 2008 Sep 1;321(1):251–62.

619 36. Kodo K, Shibata S, Miyagawa-Tomita S, Ong S-G, Takahashi H, Kume T, et al. Regulation of Sema3c
620 and the Interaction between Cardiac Neural Crest and Second Heart Field during Outflow Tract
621 Development. Sci Rep [Internet]. 2017 Jul 28 [cited 2018 Jan 8];7. Available from:
622 https://www.ncbi.nlm.nih.gov/pmc/articles/PMC5533775/

623 37. Keyte AL, Alonzo-Johnsen M, Hutson MR. Evolutionary and Developmental Origins of the Cardiac
624 Neural Crest: Building a Divided Outflow Tract. Birth Defects Res Part C Embryo Today Rev. 2014
625 Sep;102(3):309–23.

626 38. Belle M, Godefroy D, Couly G, Malone SA, Collier F, Giacobini P, et al. Tridimensional Visualization
627 and Analysis of Early Human Development. Cell. 2017 Mar;169(1):161-173.e12.

628 39. Gopalakrishnan S, Comai G, Sambasivan R, Francou A, Kelly RG, Tajbakhsh S. A Cranial Mesoderm
629 Origin for Esophagus Striated Muscles. Dev Cell. 2015 Sep;34(6):694–704.

630 40. Chotteau-Lelièvre A, Dollé P, Gofflot F. Expression Analysis of Murine Genes Using In Situ
631 Hybridization With Radioactive and Nonradioactively Labeled RNA Probes. In: Darby IA, Hewitson
632 TD, editors. In Situ Hybridization Protocols [Internet]. Totowa, NJ: Humana Press; 2006 [cited 2019
633 Jan 29]. p. 61–87. (Methods in Molecular Biology™). Available from: https://doi.org/10.1385/1-
634 59745-007-3:61

635 41. Schindelin J, Arganda-Carreras I, Frise E, Kaynig V, Longair M, Pietzsch T, et al. Fiji: an open-source
636 platform for biological-image analysis. Nat Methods. 2012 Jul;9(7):676–82.

637 42. Valente M, Resende TP, Nascimento DS, Burlen-Defranoux O, Dupont B, Cumano A, et al. HSA+
638 immature cardiomyocytes persist in the adult heart and expand after ischemic injury. bioRxiv. 2019
639 Jan 13;518530.

640

A

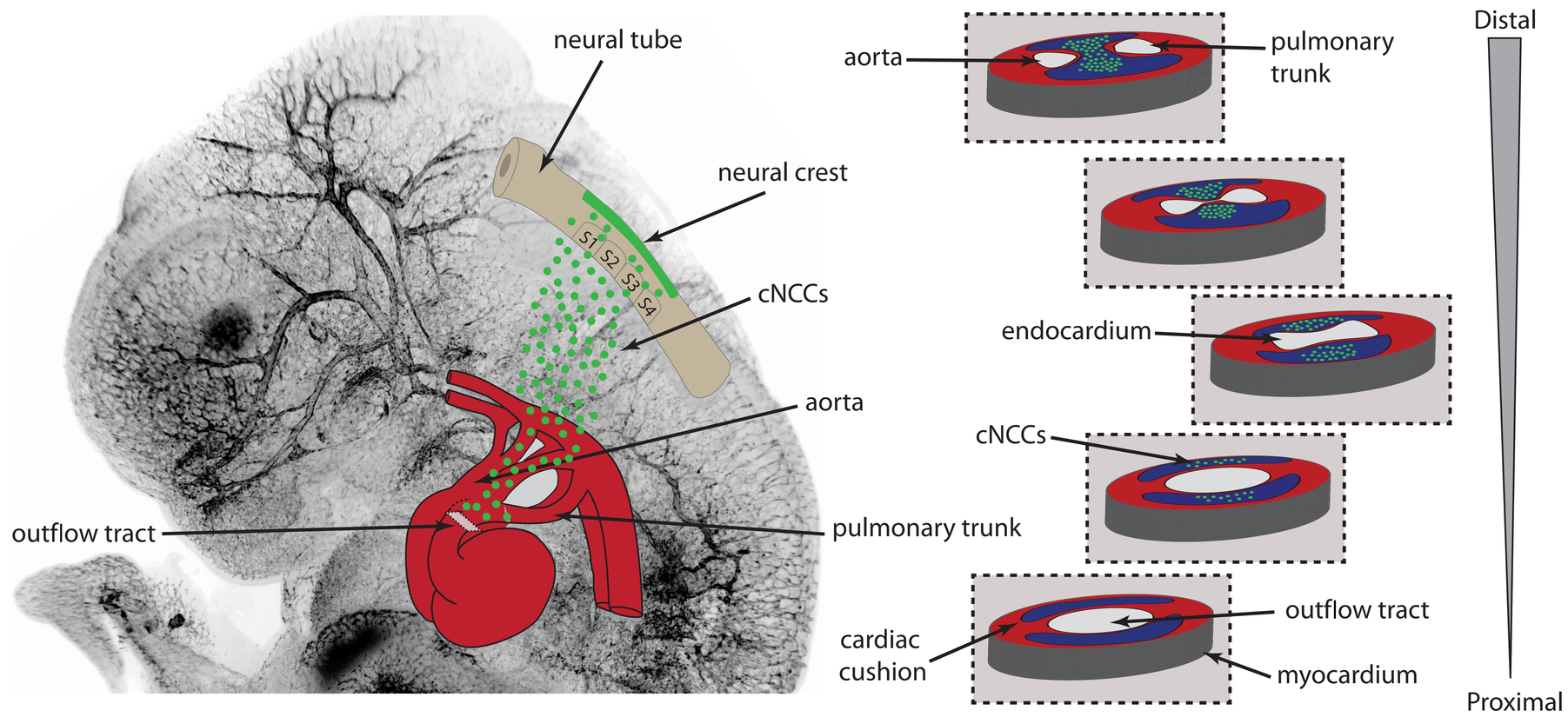
neural tube
neural crest
S1
S2
S3
S4
cNCCs
aorta
outflow tract
pulmonary trunk
aorta
pulmonary trunk
endocardium
cNCCs
cardiac cushion
outflow tract
myocardium
Distal
Proximal

B

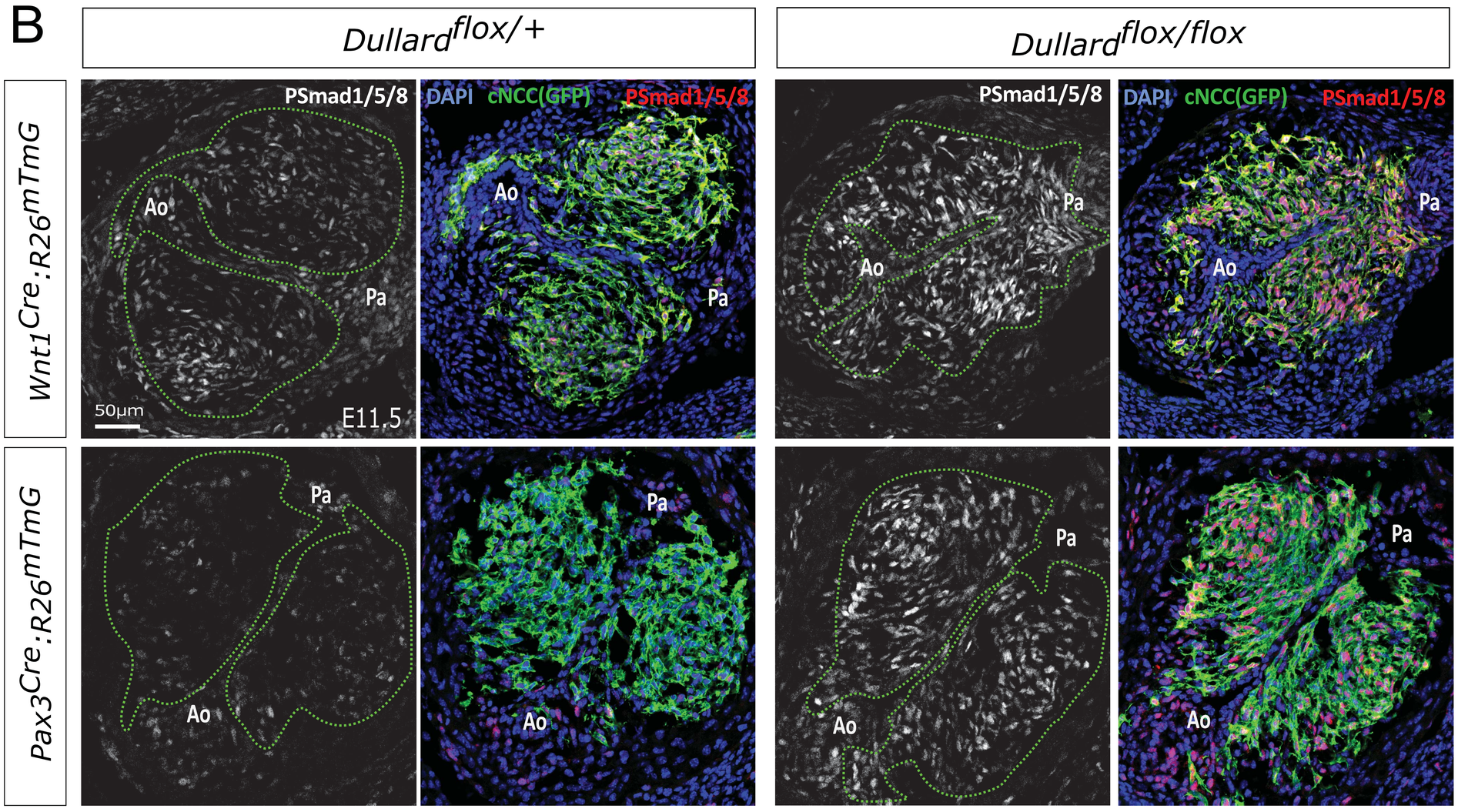
Dullard flox/+
Dullard flox/flox
Wnt1Cre;R26mTmG
Pax3Cre;R26mTmG
PSmad1/5/8
DAPI cNCC(GFP) PSmad1/5/8
Ao
Pa
50µm
E11.5

C

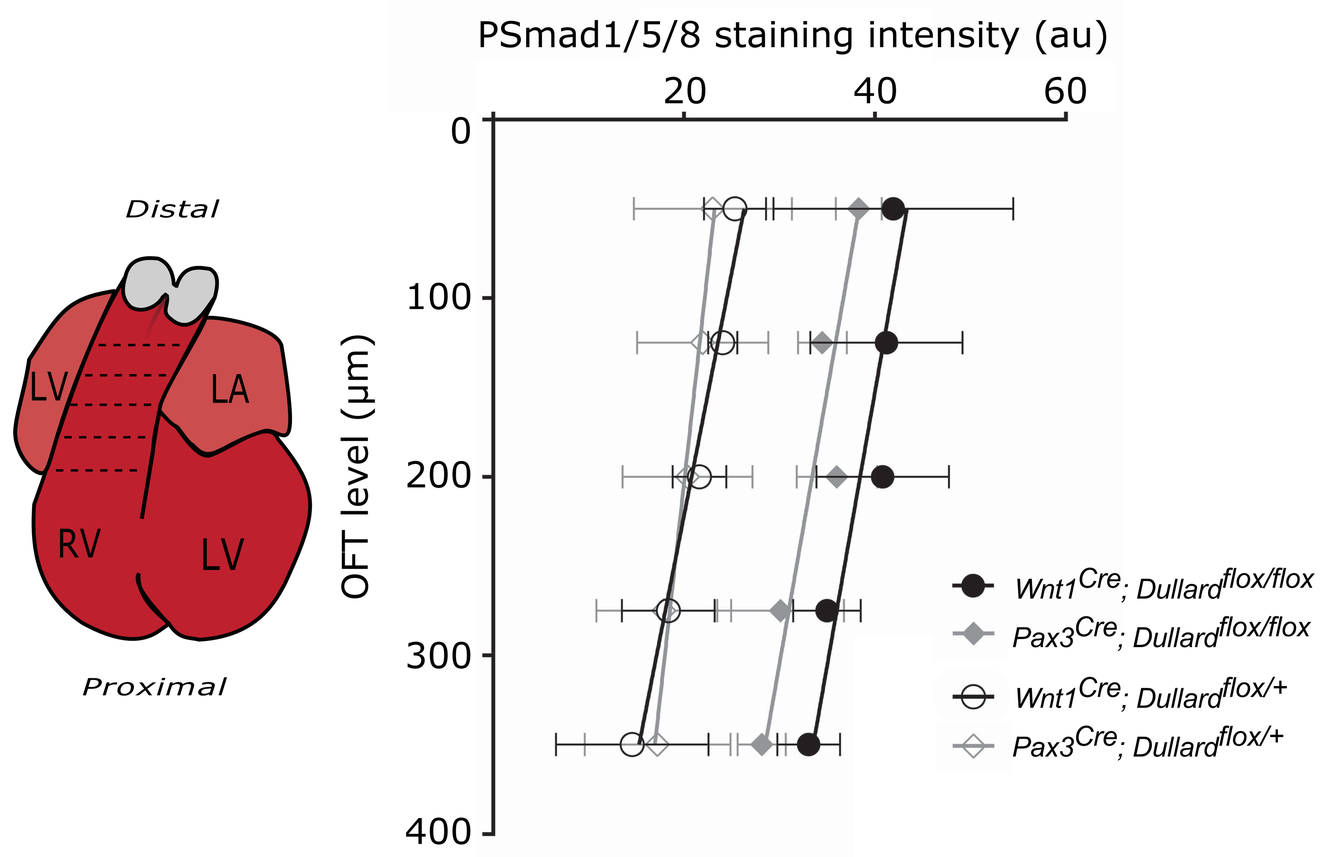
Distal
Proximal
LV
LA
RV
LV
PSmad1/5/8 staining intensity (au)
20
40
60
0
100
200
300
400
OFT level (µm)
Wnt1Cre; Dullardflox/flox
Pax3Cre; Dullardflox/flox
Wnt1Cre; Dullardflox/+
Pax3Cre; Dullardflox/+

A

Pax3^{Cre}*:Dullard*$^{+/flox}$

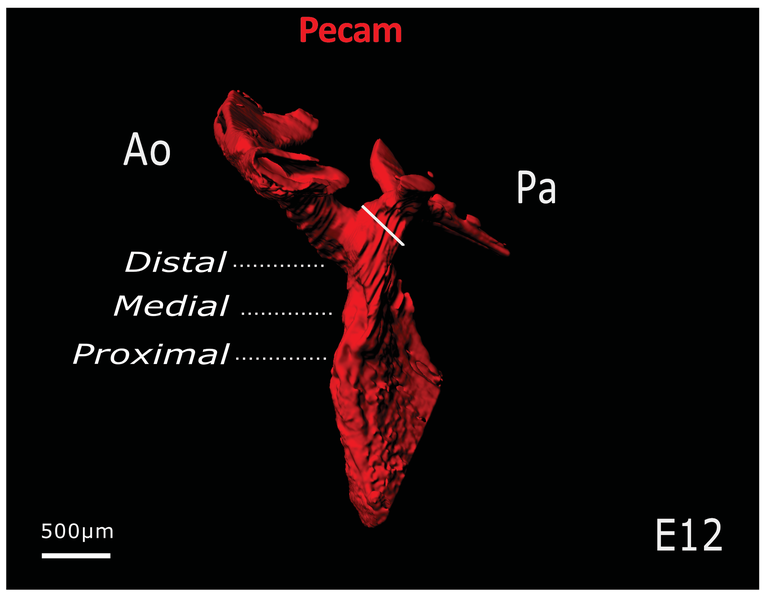

Pax3^{Cre}*:Dullard*$^{flox/flox}$

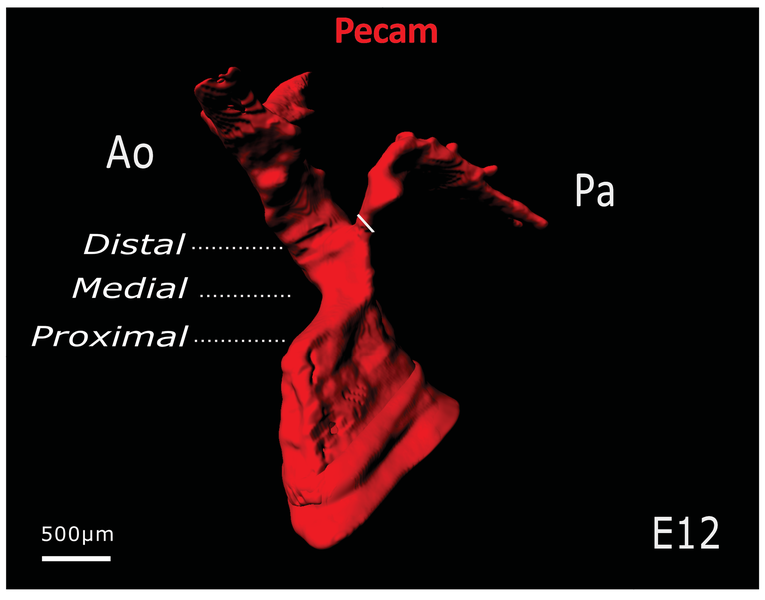

B

Wnt1^{Cre}*:R26*^{mTmG}

Dullard$^{flox/+}$ | *Dullard*$^{flox/flox}$

Pax3^{Cre}*:R26*^{mTmG}

Dullard$^{flox/+}$ | *Dullard*$^{flox/flox}$

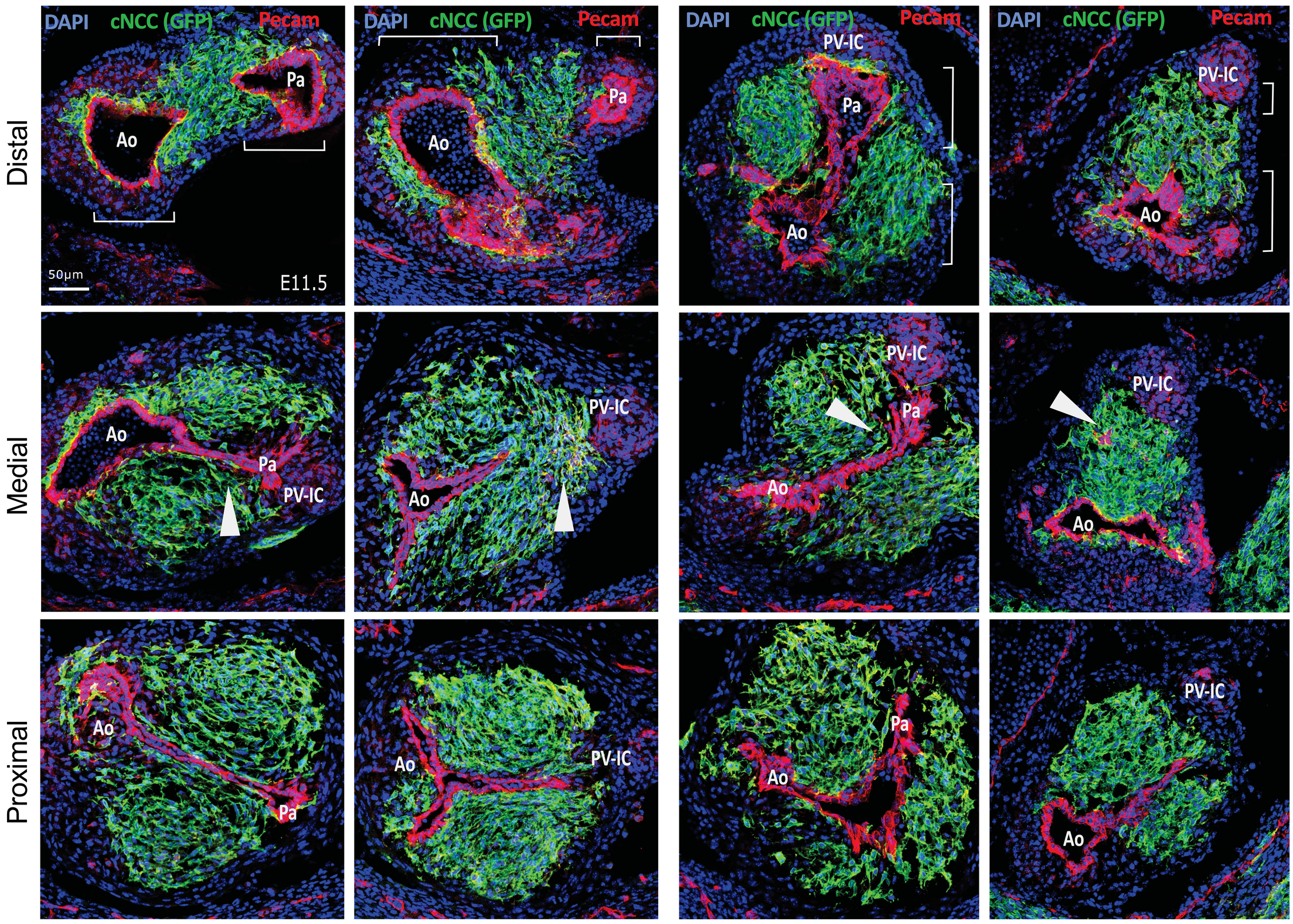

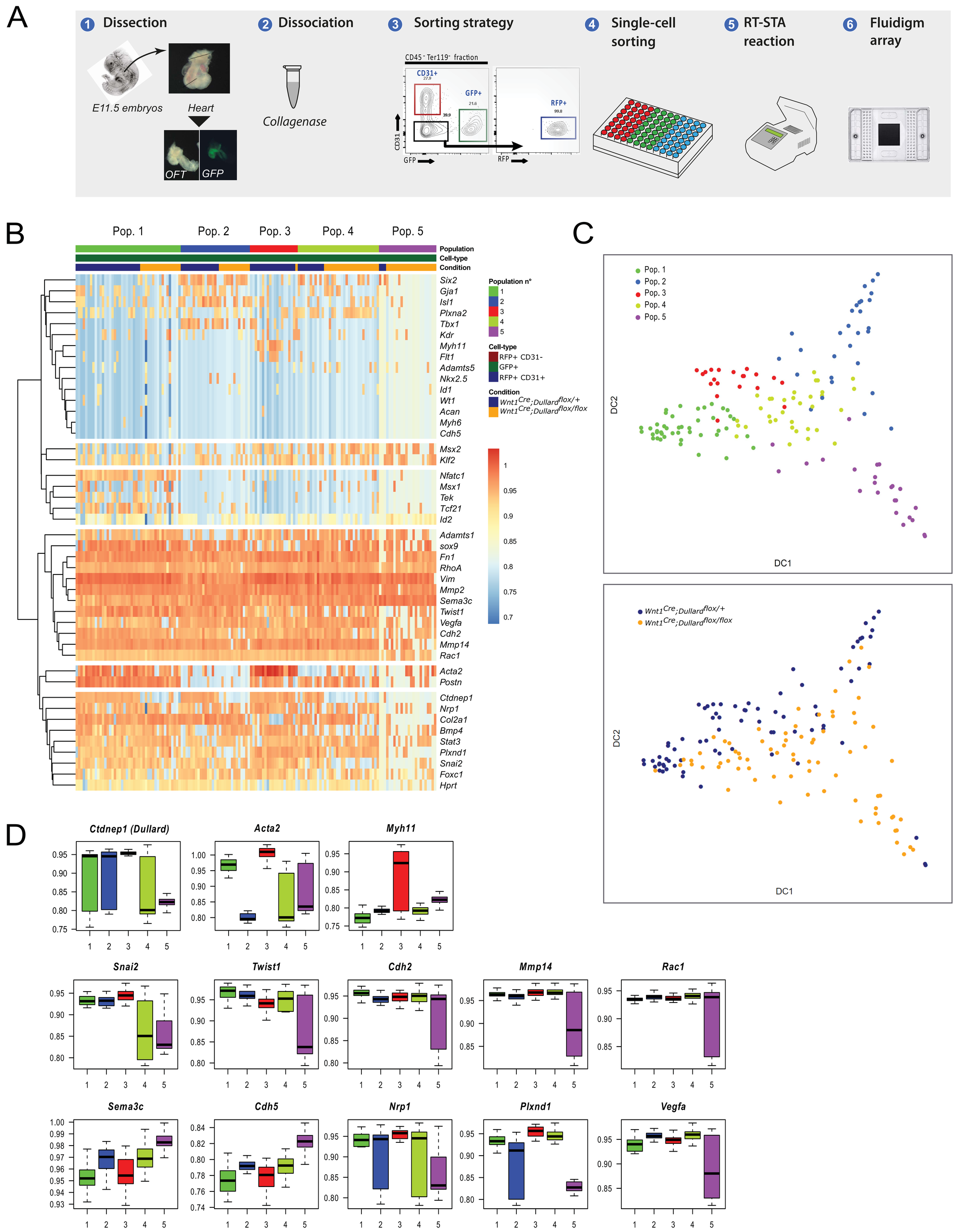
A
1 Dissection
E11.5 embryos
Heart
OFT
GFP
2 Dissociation
Collagenase
3 Sorting strategy
CD45⁻ Ter119⁻ fraction
CD31+
GFP+
RFP+
CD31
GFP
RFP
4 Single-cell sorting
5 RT-STA reaction
6 Fluidigm array
B
Pop. 1
Pop. 2
Pop. 3
Pop. 4
Pop. 5
Population
Cell-type
Condition
Six2
Gja1
Isl1
Plxna2
Tbx1
Kdr
Myh11
Flt1
Adamts5
Nkx2.5
Id1
Wt1
Acan
Myh6
Cdh5
Msx2
Klf2
Nfatc1
Msx1
Tek
Tcf21
Id2
Adamts1
sox9
Fn1
RhoA
Vim
Mmp2
Sema3c
Twist1
Vegfa
Cdh2
Mmp14
Rac1
Acta2
Postn
Ctdnep1
Nrp1
Col2a1
Bmp4
Stat3
Plxnd1
Snai2
Foxc1
Hprt
Population n°
1
2
3
4
5
Cell-type
RFP+ CD31-
GFP+
RFP+ CD31+
Condition
Wnt1Cre;Dullardflox/+
Wnt1Cre;Dullardflox/flox
C
Pop. 1
Pop. 2
Pop. 3
Pop. 4
Pop. 5
DC2
DC1
Wnt1Cre;Dullardflox/+
Wnt1Cre;Dullardflox/flox
DC2
DC1
D
Ctdnep1 (Dullard)
Acta2
Myh11
Snai2
Twist1
Cdh2
Mmp14
Rac1
Sema3c
Cdh5
Nrp1
Plxnd1
Vegfa

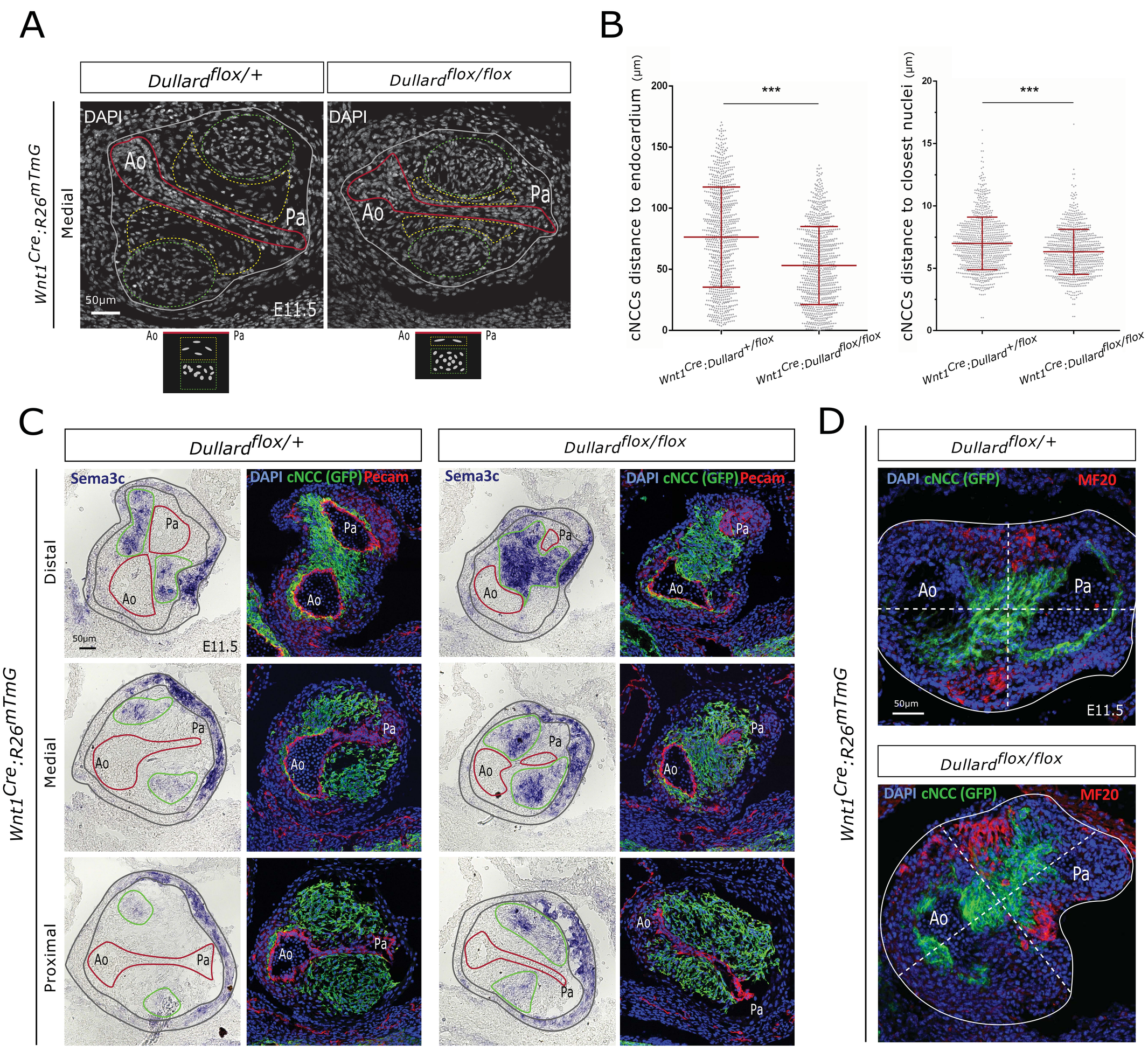
A
Dullard flox/+
Dullard flox/flox
Wnt1Cre;R26mTmG
Medial
DAPI
Ao
Pa
50µm
E11.5
B
cNCCs distance to endocardium (µm)
cNCCs distance to closest nuclei (µm)
***
Wnt1Cre;Dullard+/flox
Wnt1Cre;Dullardflox/flox
C
Distal
Medial
Proximal
Sema3c
DAPI cNCC (GFP) Pecam
D
DAPI cNCC (GFP)
MF20